

**Giant Pyroelectric Energy Harvesting and Negative Electrocaloric Effect in Multilayered Nanostructures**

Journal:	<i>Energy & Environmental Science</i>
Manuscript ID	EE-ART-12-2015-003641.R1
Article Type:	Paper
Date Submitted by the Author:	12-Jan-2016
Complete List of Authors:	Vats, Gaurav; Monash University, Mechanical Engineering Kumar, Ashok; University of Puerto Rico, Department of Physics and Institute for Functional Nanomaterials; national Physical Laboratory, Ortega, Nora; University of Puerto Rico, Department of Physics Bowen, Chris; Univ Bath, Materials Research Centre Katiyar, Ram; University of Puerto Rico, Department of Physics

Giant Pyroelectric Energy Harvesting and Negative Electrocaloric Effect in Multilayered Nanostructures

Gaurav Vats^{a,b,c*}, Ashok Kumar^{d#}, Nora Ortega^{e#}, Chris R Bowen^f and Ram S. Katiyar^{e#}

^a*IITB-Monash Research Academy, Indian Institute of Technology Bombay, Powai, India 400076*

^b*Department of Mechanical Engineering, Indian Institute of Technology Bombay, Powai, India 400076*

^c*Department of Mechanical and Aerospace Engineering, Monash University, Clayton, VIC 3800, Australia*

^d*CSIR-National Physical Laboratory, Dr. K. S. Krishnan Marg, Delhi, India 110012*

^e*Department of Physics, and Institute for Functional Nanomaterials, University of Puerto Rico, San Juan, PR 00931-3343, USA*

^f*Materials Research Centre, Department of Mechanical Engineering, University of Bath, Bath BA2 7AY, United Kingdom*

***Email:** gvats17@iitb.ac.in , er.gauravvats17@gmail.com, Phone: +91-22-2572 2545 Ext. 7500, Fax:

+91-22-2572 8675

#Authors contributed equally.

Abstract:

This work examines the potential of $\text{PbZr}_{0.53}\text{Ti}_{0.47}\text{O}_3/\text{CoFe}_2\text{O}_4$ (PZT/CFO) multi-layered nanostructures (MLNs) to achieve a giant electrocaloric effect (ECE) and enhanced pyroelectric energy harvesting. Unlike the conventional ECE, the effect in PZT/CFO MLNs is governed by a dynamic magneto-electric coupling (MEC) and can be tuned by the arrangement of the various ferroic layers. The ECE is investigated in alternate multilayers of PZT and CFO that consist of stacks of three (L3), five (L5) and nine (L9) alternating PZT and CFO layers. Intriguingly, all configurations exhibit a negative ECE, calculated using Maxwell relations, which has a high magnitude in comparison with previously reported giant negative ECE ($|\Delta T|=6.2$ K). The maximum ECE temperature change calculated in three (L3), five (L5) and nine (L9) layers is 52.3 K, 32.4 K and 25.0 K respectively. In addition, the maximum pyroelectric energy harvesting calculated for these layers using a modified Olsen cycle is four times higher than the highest reported pyroelectric energy density of $11549 \text{ kJm}^{-3}\text{cycle}^{-1}$. This increase is attributed to the cumulative effect of multiple layers that induce an enhancement in the overall polarization, 1.5 times of lead zirconate titanate, and leads to abrupt polarization changes with temperature fluctuations. The present study also sheds light on materials selection and the thermodynamic processes involved in the ECE and it is concluded that the refrigeration obtained from reversed Olsen cycle is a combined effect of an isothermal entropy as well as adiabatic temperature change.

Keywords: giant, negative electrocaloric effect, pyroelectric energy harvesting, thermodynamic cycle, materials selection

1. Introduction

Recent advancements in nanotechnology have significantly raised the demand for small scale refrigeration and energy conversion technologies. The performance of these technologies must be sufficiently high for heat extraction or recycling waste energy in integrated circuits¹, computer memories² and medical equipment³. Unfortunately the conventional vapor-cycle technologies are unable to meet these demands as they involve bulky components, such as compressors. Therefore, these emerging demands have led researchers to consider novel energy conversion systems. Among these, the electrocaloric effect (ECE)⁴⁻⁹ and pyroelectric effect¹⁰⁻¹³ based mechanisms have been considered alternatives for these applications. The electrocaloric effect is believed to be first reported in 1930¹⁴ and was later explored by US and Japan during World War-II⁸. Thereafter, the effect was not given much importance until it was observed near ferroelectric transitions of potassium dihydrogen phosphate in 1950¹⁵. This gave birth to the debate about the possibility of ECE in hydrogen-bonded materials. Later in the 1960s, with the discovery of ceramic perovskites^{16, 17}, the effect was detected at room temperature and above. Research escalated in this field after the work of Mischenko *et. al.*¹⁸ who reported a large ECE temperature change (ΔT) of 12 K at comparatively large values of applied electric field ($|\Delta E|=480 \text{ kVcm}^{-1}$) in $\text{PbZr}_{0.95}\text{Ti}_{0.5}\text{O}_3$ near its Curie temperature (495 K). The study was based on indirect measurements using Maxwell relations, which was first proposed by Thacher¹⁷. It is suggested that an entropy change (ΔS) can be calculated as an integral of change in polarization (P) with respect to temperature (T) over the applied electric field (E)^{4, 6, 19, 20}, namely,

$$\Delta S = - \int_E^{E_f} \left(\frac{\partial P}{\partial T} \right)_E dE \quad (1)$$

Further, the corresponding ECE temperature (ΔT) can be determined by,

$$\Delta T = -\frac{T}{\rho C} \int_E^{E_f} \left(\frac{\partial P}{\partial T} \right)_E dE \quad (2)$$

where, ρ and C are the density and the specific heat capacity of the material respectively. This method soon earned popularity primarily because of the convenience offered in measuring the ECE in thin films. Prior to this approach the ‘giant’ ECE temperature changes were difficult to accurately measure in thin films as the measurements were prone to influence by probe-based techniques. However, the indirect method is subjected to a few limitations which can be studied in detail elsewhere⁷. Table 1 provides the comparison for ECE in selected compositions with their corresponding operating conditions and the thermodynamic attributes, such as the applied electric field and the calculated temperature and entropy changes. It is to be noted that the ECE works as a reverse pyroelectric effect, which produces an electric charge on exposure to a thermal change.

Pyroelectric energy conversion exploits the fundamental idea of generating an electric charge due to change in remnant and/or saturation polarization as a result of thermal fluctuations. This change in polarization (P_i) with temperature change (ΔT) is given as²¹:

$$P_i = p_i \Delta T \quad (3)$$

where, p_i is the pyroelectric coefficient. Further, the induced short circuit current (I_p) for a rate of temperature change (dT/dt) can be obtained by^{21, 22}

$$I_p = A p_c \frac{dT}{dt} \quad (4)$$

where A and p_c are the surface area and the component of pyroelectric coefficient in the perpendicular direction of the electrodes, respectively. The degree of energy conversion can be significantly enhanced by adopting an appropriate operation cycle. In this context, Mohammadi

and Khodayari stressed the use of an Ericsson cycle²³. In addition, there exists a well-known variant of the Ericson cycle, termed the “Olsen cycle”²⁴⁻²⁶. The advantage of this cycle is that it operates under unipolar electric fields, rather than bipolar electric fields used in the conventional Ericson cycle, and has a comparatively reduced hysteresis loss and enhanced energy conversion. However, it is to be noted that the energy harvested using the Olsen cycle is not merely contributed by the pyroelectric effect but is also a result of the change in electrical energy storage capacity of the material with temperature. Interestingly, it has been reported that the Olsen cycle is capable of providing an energy density three orders in magnitude higher than that of obtained using the conventional pyroelectric effect²⁷. The claim has later been verified for many well-known compositions by Olsen *et. al.*^{24-26, 28-32}. Moreover, recent studies in this direction also strongly support their claim^{27, 33-42} and suggests that the Olsen cycle has particular advantages for pyroelectric based energy harvesting. Therefore, both the Olsen cycle and ECE are being extensively explored for ‘giant’ energy conversion applications. Since both methods work on the same principle, but in opposite directions, the materials requirements in order to achieve enhanced ECE or pyroelectric energy harvesting are similar.

2. Materials Selection for Giant Energy Harvesting

It is of importance to select the appropriate materials for a particular application, which requires a basic knowledge of the application domain and materials selection methodologies. Researchers have been continuously working in the direction of materials selection⁴³⁻⁴⁹ and energy harvesting^{1, 33-38, 50, 51}; and have determined the characteristics that a material should possess for high energy conversion. The material should have a large change in polarization with respect to the change in temperature ($\partial P/\partial T$), which leads to a high pyroelectric coefficient. Moreover, the

Curie temperature, dielectric anomalies, phase transitions or instantaneous switching, creation/destruction of crystal domains should generally fall within the operating temperature range. In addition, the materials should exhibit low losses, high breakdown strength and have a large change in polarization with a variation in applied electric field. Importantly, the use of thin films permits the application of high electric fields at relatively low application voltages but the electrical conductivity, which increases with a decrease in thickness, should also be sufficiently low⁶. Due to this complex combination of properties, $\text{PbZr}_{0.53}\text{Ti}_{0.47}\text{O}_3/\text{CoFe}_2\text{O}_4$ (PZT/CFO) layered nanostructures have been considered in the present study for both pyroelectric energy harvesting and ECE investigations.

3. Layered Nanostructured Materials

$\text{PbZr}_{0.53}\text{Ti}_{0.47}\text{O}_3/\text{CoFe}_2\text{O}_4$ (PZT/CFO) layered nanostructures were first reported by us in 2009⁵². Later we also investigated the temperature-dependent polarization and dielectric behavior of these layered nanostructures⁵³. Multilayered nanostructures structures (MLNs) of three (L3), five (L5) and nine (L9) alternating layers of PZT and CFO thin films were deposited on a $\text{La}_{0.5}\text{Sr}_{0.5}\text{CoO}_3$ (LSCO) coated (100) MgO substrate using pulsed laser deposition (excimer laser; laser energy density of 1.5 J cm^{-2} ; 10 Hz of repetition rate). Figure 1 (b), (c) and (d) shows the arrangements for the MLNs of L3, L5 and L9, respectively. The depositions were carried out with individual PZT and CFO targets that were initially prepared by a solid state route. Finally, the prepared MLNs were annealed and physical characterization was carried out using Raman and X-ray diffraction (XRD), see Figure S1, and transmission electron microscopy (TEM); see Figure S2. A more detailed description of the procedures and results can be found in our

previous reports^{52, 53}. These structures were found to demonstrate excellent fatigue properties with a nominal (less than 20 %) deviation in polarization over 10^8 cycles; see Figure S3. Further, dielectric measurements were carried out with sputtered Pt upper electrodes and pyroelectric properties were studied in the temperature span of 100K to 300K. The temperature dependent P - E loops obtained are highlighted in Figure 1 (a) for pure PZT (grown under the same conditions)^{52, 53} (b) L3 (c) L5 (d) L9 respectively. Intriguingly for ECE and pyroelectric harvesting applications, it is found that the polarizations of all the MLNs fall with a decrease in temperature and are completely recoverable with reheating. Normally, pure PZT films do not show any such behavior and simply result in a broadening of the loop with a decrease in temperature^{1, 52, 53}.

Another important observation is that these structures show an unusual shift in ferroelectric hysteresis loops; note the shift in the loop with a decrease in temperature in Figures 1 (b), (c) and (d). In general, the saturation polarization decreases with an increase in temperature; such a response is classified as a ‘Thermal fluctuations-1 (TF-1)’ behavior. In the present case the saturation polarization increases with an increase in temperature, termed ‘Thermal fluctuations-2 (TF-2)’ behavior where the hysteresis loop tends to become linear at low temperatures. This behavior is rare, but is observed in $(\text{Bi}_{0.5}\text{Na}_{0.5})\text{TiO}_3$, $(\text{Bi}_{0.5}\text{K}_{0.5})\text{TiO}_3$ and $(\text{Bi}_{0.5}\text{Li}_{0.5})\text{TiO}_3$ based compositions such as $0.88\text{Bi}_{0.5}\text{Na}_{0.5}\text{TiO}_3\text{-}0.02\text{SrTiO}_3\text{-}0.1\text{Bi}_{0.5}\text{Li}_{0.5}\text{TiO}_3$ (BNT-ST-BLT)⁵⁴ and $(\text{Bi}_{0.5}\text{Na}_{0.5})_{0.915}\text{-}(\text{Bi}_{0.5}\text{K}_{0.5})_{0.05}\text{Ba}_{0.02}\text{Sr}_{0.015}\text{TiO}_3$ ⁵⁵. In addition, it is also possible to have both kinds of behavior in the same composition but in different temperature ranges. The phenomena in the present case is attributed to dominance of dynamic magnetoelectric coupling (MEC) at lower temperatures^{52, 53}. Once this temperature dependent pyroelectric behavior is identified it becomes convenient to decide the possible cycle on which a device can be fabricated in order to achieve improved performance.

4. Olsen Cycle

The Olsen cycle was initially proposed in the 1980s for the commonly observed TF-1 ferroelectrics, since TF-2 compositions were rarely observed before 2008. Later (2014), the modified version of the Olsen cycle was proposed by us for TF-2 compositions³⁸. Consequently, the cycle is generalized for all materials exhibiting a change in polarization with a change in temperature³⁸. The generalized cycle states that the material should initially be polarized under a unipolar applied electric field at the lower temperature (T_L) and then exposed to a heat source isoelectrically (E_H). This leads to a polarization change (a decrease for TF-1 and increase for TF-2) that can be simultaneously converted into an electrical output. Subsequently, the material is depolarized (under a unipolar applied electric field) at a constant higher temperature (T_H) followed by an isoelectric (E_L) cooling. This again provides an output electrical impulse in the form of harvested electrical energy. Figure 2 (a) provides a schematic explanation of a typical Olsen cycle for a TF-2 material and the corresponding T - S diagram is shown in Figure 2 (b). This cycle consists of two isoelectric (B - C and D - A) and two isothermal processes (A - B and C - D) as discussed below:

Process A - B (Isothermal polarization): The material is polarized from P_A to P_B by using a unipolar electric field (E_L to E_H) at a constant temperature T_L (lower temperature). This simultaneously causes an isothermal entropy reduction from S_A to S_B .

Process B - C (Isoelectric heating): In this stage the temperature of the material is raised (from T_L to T_H) or the heat is absorbed by the material isoelectrically causing a polarization rise (P_B to P_C) and a corresponding entropy decrease from S_B to S_C .

Process C - D (Isothermal depolarization): The material is depolarized isothermally at a constant higher temperature (T_H).

Process $D-A$ (Isoelectric cooling): Finally, the cycle is completed by cooling the material at a constant lower electric field (E_L) so as to bring the system to its initial state (T_L , P_A and S_A).

The area enclosed ($A-D-C-D$) by the complete cycle on a corresponding $P-E$ curve gives the net harvested output electrical energy density (N_D) per liter per unit cycle^{31,39}.

$$N_D = \oint E.dP \quad (5)$$

A careful examination of the $T-S$ diagram for Olsen cycle suggests that if the cycle is operated in a reverse direction it will result in refrigeration³⁸. At this point, it is important to note that for a material to work with a practical Olsen cycle an arrangement is needed to achieve specialized oscillating heat currents and an external load circuit is required for receiving an electrical output. A variation in the design of such an arrangement can significantly influence the degree of harvested electrical energy density.

7. Reversed Olsen Cycle for Refrigeration

Recently, it was proposed that the Olsen cycle operated in the reverse direction can be used for refrigeration³⁸. The cycle again consists of two isoelectric ($B-C$ and $D-A$) and two isothermal processes ($A-B$ and $C-D$). Figure 3 (a) and (b) shows the $P-E$ and $T-S$ diagrams for the working of a reversed Olsen cycle. The cycle is comprised of the following steps:

Process $A-B$ (Isothermal polarization): The material is polarized from P_A to P_B using a unipolar electric field (E_L to E_H) at a constant temperature T_H (higher temperature). This simultaneously causes an isothermal entropy reduction from S_A to S_B . It is to be noted that S_B corresponds to the state of least saturation entropy of the system for the temperature T_H .

Process B-C (Isoelectric refrigeration): As the material has already achieved the state of least entropy or the lower saturation limit of the entropy, it undergoes a temperature change (T_H to T_L) in order to have a higher entropy state. Therefore, the material releases heat and cools itself to achieve a higher entropy state (S_C) at a constant electric field (E_H). This process also causes a decrease in polarization (P_B to P_C).

Process C-D (Isothermal depolarization): In this process the material is further depolarized isothermally at a constant lower temperature (T_L).

Process D-A (Isoelectric heat exchange): In order to complete the cycle the material is allowed to exchange heat with the surroundings at a constant lower electric field (E_L). This step provides an opportunity for the material to attain its original state (T_L , P_A and S_A) by absorbing heat from the surroundings. Depending on the materials behavior it may absorb heat itself or may be forced to do so in the presence of an external heat source.

Interestingly, the material cools during process B-C while gains heat during process D-A; note the heating and cooling of the material in Figure 4. Normally, the surroundings are heated in process B-C and refrigerated in process D-A (note the heating and cooling of the surroundings in Figure 3). Therefore, depending on the application requirements this cycle can be used to cool the material or the surroundings; it is important to note that the effect of producing thermal changes under varying applied electric fields is also known as ECE⁸. The T - S diagram (Figure 3(b)) for the reversed Olsen cycle also confirms that the cycle is working in an identical way to that of ECE in a three stage thermodynamic model (isoelectric, isothermal and adiabatic processes)⁶.

8. Results and Discussion

Figure 3 and 4 clearly indicates that the processes $A-B$ and $C-D$ are essentially isothermal while the processes $B-C$ and $D-A$ are isoelectric. This makes it is difficult to describe the adiabatic process involved in the cycle which is often used to explain the ECE. This can be better understood on the basis of the concept of entropy. The net entropy (S_N) of the system can be written as the sum of entropy due to polarization ($S_{E,T}$ – a function of both temperature and electric field) and entropy due to lattice parameters and electron contribution (S_T – a function of temperature only). The net entropy (ΔS_N) change of the system can be written as

$$\Delta S_N = \Delta S_{E,T} + \Delta S_T \quad (7)$$

Eq.7 clearly suggests that a change in temperature will influence all entropies of the system while a change in applied electric field will merely influence the entropy of polarization. Based on this concept we can understand that during isothermal polarization (process $A-B$) the $\Delta S_{E,T}$ decreases and the overall entropy of the system should fall from S_A to S_B . Consequently, the system must release heat thereby leading to cooling of the material; this is often attributed as an adiabatic ECE⁶. At the same time there is no change in ΔS_T since it is independent of applied electric field and hence the process becomes partially adiabatic. Finally, process $A-B$ brings the material to the state of least entropy (S_B); see figure 4 and 3 (b). At this stage the material is kept at a constant electric field and hence the entropy of polarization ($\Delta S_{E,T}$) does not change. This means the process should be adiabatic. However, the material attempts to achieve a state of higher entropy due to lattice strains developed during high temperature polarization. As a result, the net entropy (ΔS_N) rises in process $B-C$. If ΔS_N rises (S_B to S_C) under adiabatic conditions the system has to undergo a temperature change (T_H to T_L), this again leads to cooling of the

material (and heat gained by the surroundings); see figure 4. In addition, the temperature change also causes ΔS_T to fluctuate which violates the condition of an adiabatic process. This makes it difficult to describe the overall nature of the two kinds of cooling involved and therefore both processes (corresponding to ΔS_T and ΔS_{ET}) are collectively considered as partially adiabatic and are accounted for in the ECE. Here, it is important to note that the cooling obtained in both the processes ($A-B$ and $B-C$) can be attributed as an ECE. The cooling in process $A-B$ is universal and can be found in any material that exhibits an electric field dependent polarization change while the latter is dependent on the materials' structure and is therefore an intrinsic property of a material. Thus it can be concluded that the reversed Olsen cycle takes advantage of the latter type of cooling process for enhanced performance and is a potential mechanism for some materials to exhibit a 'giant' ECE. This suggests that the refrigeration obtained from reversed Olsen cycle is a combined effect of isothermal entropy and adiabatic temperature change. The same argument in a reverse manner makes the Olsen cycle to perform better with regards to the pyroelectric effect.

As discussed earlier, the present study considers PZT/CFO MLNs since they satisfy most of the essential characteristics required for giant ECE and colossal energy harvesting density using the Olsen cycle. These MLNs of L3, L5 and L9 are investigated for the temperature spectrum of 100 K to 300 K and applied electric field of 0-400 kVcm⁻¹. The indirect ECE calculations are carried out using Maxwell relations (equations 1 and 2). In this context, experimental values obtained from the upper branches (polarization variation from remnant to saturation polarization in the first quadrant) of $P-E$ isotherms are used to plot isoelectric $P-T$ curves (Figure 5). Here, a sharp increase in the polarization is observed as the temperature increases to approximately 200 K. Such a phenomenon in multilayered structures is often attributed to structural transitions or space

charge effects at surface/interface; but this is not thought to be the case for the MLNs as verified by the nominal (less than 20 %) change in polarization over large time span of fatigue test (tested over 10^8 cycles⁵³); see Figure S3. Therefore, the main reason for this behavior is the electrical dominance of dynamic magnetoelectric coupling (MEC)^{52, 53, 56}. The MEC is referred to as a switching among more than one ferroic order parameters leading to a rise in a certain physical properties such as ferroelectric/electric control of magnetization or vice-versa⁵⁷. The effect has been investigated using Ginzburg–Landau theory and it is found that the MEC in these MLNs is stronger at lower temperatures and becomes weaker at higher temperatures⁵³. At an elevated temperature (>200 K), the polarization enhancement is relatively low due to a weak MEC. A significant increase in magnetization below 200 K drastically switches the polarization due to a strong magneto-electric coupling which in turn switches the polarization and hence produces large ECE effects⁵³. This reason makes the investigation of ECE intriguing in the MEC governed polarization switch. Furthermore, calculations of the entropy (ΔS) and temperature (ΔT) change are performed using a standard procedure⁵⁸ that ensures the reliability of the Maxwell calculations²⁰ using the P - T plots illustrated in Figure 5. The calculations are performed for $\rho=8.3$ gcm⁻³ and $C=330$ JK⁻¹kg⁻¹ (assumed constant with variation in temperature)⁵⁹. Figure 6 (a), (b) and (c) shows the calculated entropy-temperature (ΔS - T) results while ECE temperature change-temperature (ΔT - T) curves are revealed in Figure 6 (d), (e) and (f) for L3, L5 and L9, respectively; the values are calculated using Eqns. 1 and 2. All structures are found to illustrate a negative ECE where L3 accommodates the maximum temperature change of 52.2 K ($|\Delta S|=94.23$ Jkg⁻¹K⁻¹; $|\Delta E|=370$ kVcm⁻¹) at 182 K followed by L5 with $|\Delta T|=30.41$ K ($|\Delta S|=53.88$ Jkg⁻¹K⁻¹ $|\Delta E|=370$ kVcm⁻¹) at 186 K. To best of the author's knowledge the discovered indirect ECE in MLNs of PLZT/CFO is the maximum ECE reported to date (see Table 1). The table suggests

that these MLNs also have a very high $|\Delta T/\Delta E|$ ratio, which is often considered a criterion for comparing the ECE performance of different materials⁶⁰. However, it is to be noted that the ECE is also dependent on time and the polarization values may decay with time. It has been reported that this could lead to variation in calculated entropy and temperature change by a factor of two⁶¹. Even if the effect of time is considered the ECE in reported MLNs is highest. Another important observation is the decrease in ECE with layer addition due to a lowering of the net polarization. This may be due to enhanced inter-layer strain and formation of dead layers across the interface with increase in number of ferroelectric (FE) and ferromagnetic (FM) layers which causes a decrease in polarization; note the difference in saturation polarization of all the layers is given in Figure 1. This finally leads to a reduced ECE as the effect is dependent on change in polarization with temperature, as indicated by equations 1 and 2. However, at the same time the temperature corresponding to the maximum ECE also increases (205 K: L9; 186 K: L5; 182 K: L3) with an increase in the number of layers. This suggests that the ECE can be tuned by arrangement and the number of the layers. The exceptional ECE results also make these MLNs appealing for the complementary application of pyroelectric energy harvesting.

All three MLNs are analyzed for energy harvesting using the Olsen cycle. Figure 7 (a) shows the variation of energy density for all three configurations (using eq. 5). These are found to have a maximum energy density of 23011 (L9), 35278 (L5) and 47372 (L3) kJm^{-3} respectively. The estimated energy densities obtained are higher than any existing ‘giant’ value reported to date. Table 2 shows a comparison of energy density and corresponding conditions for selected compositions reported for giant energy harvesting using the Olsen cycle. The reason for this large increase is due to dynamic ME effects in these structures (see the difference in polarization of pure PZT and MLNs (Figure 1)) that cause an increase in the polarization. Additionally,

Figure 7 (b), (c) and (d) shows information regarding the energy harvesting behavior as a function of E_H with both E_L and T_L kept constant at 0 kVcm^{-1} and 100 K respectively. The trend illustrate that the energy density increases with a broadening of the temperature range and electric field. However, the dominant magnetism at low temperatures may result in a deviation from the presented energy densities. The change is significantly low due to nominal energy losses (due to increased magnetic polarization) while polarizing at 100 K ^{52, 53}. Though the present case has very low magnetic losses, there may be cases of large magnetic deviation in some MLNs. Such cases can be dealt by simultaneously coupling the Olsen cycle and its similar counterpart in the magnetic domain and we are exploring such possibilities. In summary, this study demonstrates the competence of MLNs for EC refrigeration and pyroelectric energy harvesting and highlights new opportunities and directions in the domain of solid state energy conversion.

Conclusions

PZT/CFO multilayered nanostructures (MLNs) are revealed to provide exceptional potential for electrocaloric refrigeration and pyroelectric energy harvesting. From the indirect mode of measurement, these structures are found to illustrate giant negative ECE (L3: $|\Delta T|=52.2 \text{ K}$; L5: $|\Delta T|=30.4 \text{ K}$; L9: $|\Delta T|=25.0 \text{ K}$ at $T=182, 186$ and 205 K respectively), the largest reported to date. At the same time a shift in the temperature corresponding to maximum ECE can also be observed with an increase in number of layers (205 K : L9; 186 K : L5; 182 K : L3). This suggests that the ECE can be tuned by using multi-layers and the arrangement of the layers. Additionally, the estimated energy harvesting potential of these layers is also found to be large (L3: $47372 \text{ kJm}^{-3}\text{cycle}^{-1}$; L5: $35278 \text{ kJm}^{-3}\text{cycle}^{-1}$; L3: $23011 \text{ kJm}^{-3}\text{cycle}^{-1}$) and is higher than the maximum

reported values to date. The present study also helps in understanding the three stage (adiabatic, isothermal and isoelectric) thermodynamic processes involved in ECE for such materials.

References

1. C. Bowen, J. Taylor, E. LeBoulbar, D. Zabek, A. Chauhan and R. Vaish, *Energy & Environmental Science*, 2014.
2. D. S. Holmes, A. L. Ripple and M. A. Manheimer, *Applied Superconductivity, IEEE Transactions on*, 2013, **23**, 1701610-1701610.
3. G. B. Altshuler, J. P. Caruso, H. H. Zenzie, J. G. Burke III and A. V. Erofeev, *Journal*, 2012.
4. T. Correia, S. Kar-Narayan, J. Young, J. Scott, N. Mathur, R. W. Whatmore and Q. Zhang, *Journal of Physics D: Applied Physics*, 2011, **44**, 165407.
5. X. Li, S.-G. Lu, X.-Z. Chen, H. Gu, X.-s. Qian and Q. Zhang, *Journal of Materials Chemistry C*, 2013, **1**, 23-37.
6. J. Scott, *Annual Review of Materials Research*, 2011, **41**, 229-240.
7. M. Valant, *Progress in Materials Science*, 2012, **57**, 980-1009.
8. X. Moya, S. Kar-Narayan and N. Mathur, *Nature materials*, 2014, **13**, 439-450.
9. X. Moya, E. Defay, V. Heine and N. D. Mathur, *Nature Physics*, 2015, **11**, 202-205.
10. D. Guyomar, S. Pruvost and G. Sebald, *Ultrasonics, Ferroelectrics and Frequency Control, IEEE Transactions on*, 2008, **55**, 279-285.
11. M. Ikura, *Ferroelectrics*, 2002, **267**, 403-408.
12. A. Khodayari, S. Pruvost, G. Sebald, D. Guyomar and S. Mohammadi, *Ultrasonics, Ferroelectrics and Frequency Control, IEEE Transactions on*, 2009, **56**, 693-699.
13. L. Kouchachvili and M. Ikura, *International Journal of Energy Research*, 2008, **32**, 328-335.
14. P. Kobeko and J. Kurtschatov, *Zeitschrift für Physik A Hadrons and Nuclei*, 1930, **66**, 192-205.
15. H. Baumgartner, Diss. Naturwiss. ETH Zürich, Nr. 1905, 0000. Ref.: Scherrer, P.; Korref.: Busch, G., 1950.
16. A. Karchevskii, *Soviet Physics-Solid State*, 1962, **3**, 2249-2254.
17. P. Thacher, *Journal of applied physics*, 1968, **39**, 1996-2002.
18. A. Mischenko, Q. Zhang, J. Scott, R. Whatmore and N. Mathur, *Science*, 2006, **311**, 1270-1271.
19. W. Eerenstein, N. Mathur and J. F. Scott, *Nature*, 2006, **442**, 759-765.
20. W. Geng, Y. Liu, X. Meng, L. Bellaiche, J. F. Scott, B. Dkhil and A. Jiang, *Advanced Materials* 2015, **27**, 3165-3169.
21. R. Whatmore, *Ferroelectrics*, 1991, **118**, 241-259.
22. R. Whatmore, *Reports on progress in physics*, 1986, **49**, 1335.
23. S. Mohammadi and A. Khodayari, *Smart Materials Research*, 2012, **2012**.
24. R. Olsen and D. Bruno, 1986.
25. R. B. Olsen, D. A. Bruno and J. M. Briscoe, *Journal of applied physics*, 1985, **58**, 4709-4716.
26. R. B. Olsen, D. A. Bruno, J. M. Briscoe and E. W. Jacobs, *Journal of applied physics*, 1985, **57**, 5036-5042.
27. R. Kandilian, A. Navid and L. Pilon, *Smart Materials and Structures*, 2011, **20**, 055020.
28. R. Olsen and D. Brown, *Ferroelectrics*, 1982, **40**, 17-27.
29. R. Olsen, D. Bruno, J. Briscoe and J. Dullea, *Ferroelectrics*, 1984, **59**, 205-219.

30. R. B. Olsen, *Journal of Energy*, 1982, **6**, 91-95.
31. R. B. Olsen, J. M. Briscoe, D. A. Bruno and W. F. Butler, *Ferroelectrics*, 1981, **38**, 975-978.
32. R. B. Olsen and D. Evans, *Journal of applied physics*, 1983, **54**, 5941-5944.
33. A. Chauhan, S. Patel, G. Vats and R. Vaish, *Energy Technology*, 2014, **2**, 205-209.
34. R. Sao, G. Vats and R. Vaish, *Ferroelectrics*, 2015, **474**, 1-7.
35. G. Vats, A. Chauhan and R. Vaish, *International Journal of Applied Ceramic Technology*, 2015, **12**, E49-E54.
36. G. Vats, H. S. Kushwaha and R. Vaish, *Materials Research Express*, 2014, **1**, 015503.
37. G. Vats, H. S. Kushwaha, R. Vaish, N. A. Madhar, M. Shahabuddin, J. M. Parakkandy and K. M. Batoo, *Journal of Advanced Dielectrics*, 2014, **4**.
38. G. Vats, R. Vaish and C. R. Bowen, *Journal of applied physics*, 2014, **115**, 013505.
39. F. Y. Lee, S. Goljahi, I. M. McKinley, C. S. Lynch and L. Pilon, *Smart Materials and Structures*, 2012, **21**, 025021.
40. F. Y. Lee, A. Navid and L. Pilon, *Applied thermal engineering*, 2012, **37**, 30-37.
41. I. M. McKinley, R. Kandilian and L. Pilon, *Smart Materials and Structures*, 2012, **21**, 035015.
42. A. Navid, C. S. Lynch and L. Pilon, *Smart Materials and Structures*, 2010, **19**, 055006.
43. G. Vats, *Multi-Attribute Decision Making for Ferroelectric Materials Selection*, Lambert Academic Publishers, 2014.
44. G. Vats and R. Vaish, *Journal of Advanced Ceramics*, 2013, **2**, 141-148.
45. G. Vats and R. Vaish, *Journal of Asian Ceramic Societies*, 2014, **2**, 5-10.
46. G. Vats and R. Vaish, *Advanced Science Focus*, 2014, **2**, 140-147.
47. G. Vats and R. Vaish, *International Journal of Applied Ceramic Technology*, 2014, **11**, 883-893.
48. G. Vats, R. Vaish and C. R. Bowen, *International Journal of Applied Ceramic Technology*, 2015, **12**, E1-E7.
49. G. Vats, M. Sharma, R. Vaish, V. S. Chauhan, N. A. Madhar, M. Shahabuddin, J. M. Parakkandy and K. M. Batoo, *Ferroelectrics*, 2015, **481**, 64-76.
50. G. Vats, S. Patel, A. Chauhan and R. Vaish, *International Journal of Applied Ceramic Technology*, 2015, **12**, 765-770.
51. C. Bowen, H. Kim, P. Weaver and S. Dunn, *Energy & Environmental Science*, 2014.
52. N. Ortega, A. Kumar, R. S. Katiyar and C. Rinaldi, *Journal of Materials Science*, 2009, **44**, 5127-5142.
53. N. Ortega, A. Kumar, R. S. Katiyar and C. Rinaldi, *Thin Solid Films*, 2010, **519**, 641-649.
54. D. Lin, K. Kwok and H. Chan, *Journal of alloys and compounds*, 2009, **481**, 310-315.
55. D. Lin and K. W. Kwok, *Journal of the American Ceramic Society*, 2010, **93**, 806-813.
56. G. Vats, A. Kumar, R. S. Katiyar and N. Ortega, *arXiv preprint arXiv:1512.08888*, 2015.
57. V. Garcia, M. Bibes, L. Bocher, S. Valencia, F. Kronast, A. Crassous, X. Moya, S. Enouz-Vedrenne, A. Gloter and D. Imhoff, *Science*, 2010, **327**, 1106-1110.
58. A. Mischenko, Q. Zhang, J. Scott, R. Whatmore and N. Mathur, *Science*, 2006, **311**, 1270-1271.
59. M. Saad, P. Baxter, R. Bowman, J. Gregg, F. Morrison and J. Scott, *Journal of Physics: Condensed Matter*, 2004, **16**, L451.
60. E. Defay, S. Crossley, S. Kar-Narayan, X. Moya and N. D. Mathur, *Advanced Materials*, 2013.
61. S. Rowley, M. Hadjimichael, M. Ali, Y. Durmaz, J. Lashley, R. Cava and J. Scott, *arXiv preprint arXiv:1410.2908*, 2014.
62. S. Lu, B. Rožič, Q. Zhang, Z. Kutnjak, X. Li, E. Furman, L. J. Gorny, M. Lin, B. Malič and M. Kosec, *Applied physics letters*, 2010, **97**, 162904.
63. X. Hao and J. Zhai, *Applied physics letters*, 2014, **104**, 022902.
64. X. Hao, Z. Yue, J. Xu, S. An and C.-W. Nan, *Journal of applied physics*, 2011, **110**, 064109.
65. X. Hao, Y. Zhao and Q. Zhang, *The Journal of Physical Chemistry C*, 2015, **119** 18877-18885.

66. M. H. Park, H. J. Kim, Y. J. Kim, T. Moon, K. Do Kim and C. S. Hwang, *Nano Energy*, 2015, **12**, 131-140.
67. M. H. Park, Y. H. Lee, H. J. Kim, Y. J. Kim, T. Moon, K. D. Kim, J. Müller, A. Kersch, U. Schroeder and T. Mikolajick, *Advanced Materials*, 2015, **27**, 1811-1831.
68. Y. Bai, G.-P. Zheng, K. Ding, L. Qiao, S.-Q. Shi and D. Guo, *Journal of applied physics*, 2011, **110**, 094103.
69. X.-C. Zheng, G.-P. Zheng, Z. Lin and Z.-Y. Jiang, *Thin Solid Films*, 2012, **522**, 125-128.
70. F. Le Goupil, A. Berenov, A.-K. Axelsson, M. Valant and N. M. Alford, *Journal of applied physics*, 2012, **111**, 124109.
71. Y. Bai, G.-P. Zheng and S.-Q. Shi, *Materials research bulletin*, 2011, **46**, 1866-1869.
72. X. Jiang, L. Luo, B. Wang, W. Li and H. Chen, *Ceramics international*, 2014, **40**, 2627-2634.
73. R. Pirc, B. Rožič, J. Koruza, B. Malič and Z. Kutnjak, *EPL (Europhysics Letters)*, 2014, **107**, 17002.
74. G. Sebald, S. Pruvost and D. Guyomar, *Smart Materials and Structures*, 2008, **17**, 015012.
75. X. Hao, Y. Zhao and S. An, *Journal of the American Ceramic Society*, 2015, **98**, 361-365.

Table 1: Comparison of ECE in selected compositions.

Material	T [K]	ΔT [K]	ΔS [Jkg ⁻¹ K ⁻¹]	ΔE [kVcm ⁻¹]	$ \Delta T / \Delta E $ [KcmkV ⁻¹]	Reference
PZT95/05 [^]	495	12	8	480	0.0250	58
PLZT8/65/35 [^]	318	40	50	1200	0.0333	62
PLZST [^]	305	3.8	-	80	0.0475	63
SrBi ₂ Ta ₂ O ₉ [^]	565	4.9	2.4	600	0.0082	8
PBZ [^]	290	45	47	598	0.0753	8
PLZT2/95/05 [#]	493	8.5	-	754	0.0113	64
PLZST	306	33	-	900	0.0366	65
Hf _{0.2} Zr _{0.8} O ₂	307	13.4	-	3260	0.004	66, 67
PZO [#]	508	7.7	-	514	0.0150	64
PNZST [^]	323	5.5	-	139	0.0396	63
BT [#]	353	7.1	-	800	0.0089	68
BNT-0.1BT*	323	-3.3	-	517	0.0064	69
PMN-0.30PT*	353	-0.15	-	10	0.0150	70

BNT*	298	-0.12	-0.0096	50	0.0024	71
NBT*	293	-1.6	-	70	0.0229	72
PZO*	310	-1.05	-	100	0.0105	73
PLZT2/95/05*[^]	303	-5	-	308	0.0162	20
PST*	341	-6.2	-6.3	774	0.0080	4
PZT/CFO-L9[^]	205	-25	-40.16	370	0.0675	Present work
PZT/CFO-L5[^]	186	-30.41	-53.88	370	0.0821	Present work
PZT/CFO-L3[^]	182	-52.2	-94.23	370	0.1411	Present work

*Negative EC effect; [#]Thick Films; [^]Thin films; the negative sign indicates a negative electrocaloric effect.

Table 2: Comparison of energy density and corresponding conditions for selected compositions.

Material	T_{Low} (K)	T_{High} (K)	E_{Low} (MVm⁻¹)	E_{High} (MVm⁻¹)	Energy Density (kJm⁻³cycle⁻¹)	Reference
73/27 P(VDF-TrFE)[^]	296	340	23	53	30	26
PZN-4.5PT	373	433	0	2.0	217	12
PZN-5.5PT	373	463	0	1.2	150	74
PMN-10PT	303	353	0	3.5	186	74
PMN-32PT	353	443	0	0.9	100	27
60/40 P(VDF-TrFE)[^]	331	350	4.1	47.2	52	11
PNZST	418	448	0.8	3.2	300	25
8/65/35 PLZT[#]	298	433	0.2	7.5	888	39
BNT-ST-BLT	293	413	0.1	6	2130	34
KNTM	413	433	0.15	0.15	629	35
BNLT	298	393	0.1	11.2	1146	33
BNKT	298	383	0.1	5.2	1986	33

BNK-BST	293	433	0.1	4.0	1523	38
PLZST (x=0.2)[#]	293	493	30	40	6800	65
YBFO[^]	15	300	0.1	4	7570	36
PLZST (x=0.18)[#]	298	573	30	90	7800	75
0.67PMN-0.33PT[^]	303	323	0	60	6500	37
0.68PMN-0.32PT[^]	303	323	0	60	8000	37
Hf_{0.2}Zr_{0.8}O₂	273	423	0	326	11549	66, 67
PZT/CFO-L9[^]	100	300	0	40	23011	Present work
PZT/CFO-L5[^]	100	300	0	40	35278	Present work
PZT/CFO-L3[^]	100	300	0	40	47372	Present work

[#]Thick Films; [^]Thin Films

Figure Captions

Figure 1: Temperature dependent polarization versus electric field (P - E) behavior of (a) pure PZT thin films, (b) L3, (c) L5 and (d) L9 MLNs^{52, 53}. Note the increase in polarization with an increase of temperature.

Figure 2: (a) Isothermal unipolar electric polarization versus electric field (P - E) hysteresis loops (b) temperature versus entropy (T - S) curves for electrical energy harvesting (A-B-C-D) using Olsen cycle operated between different temperatures T_L and T_H .

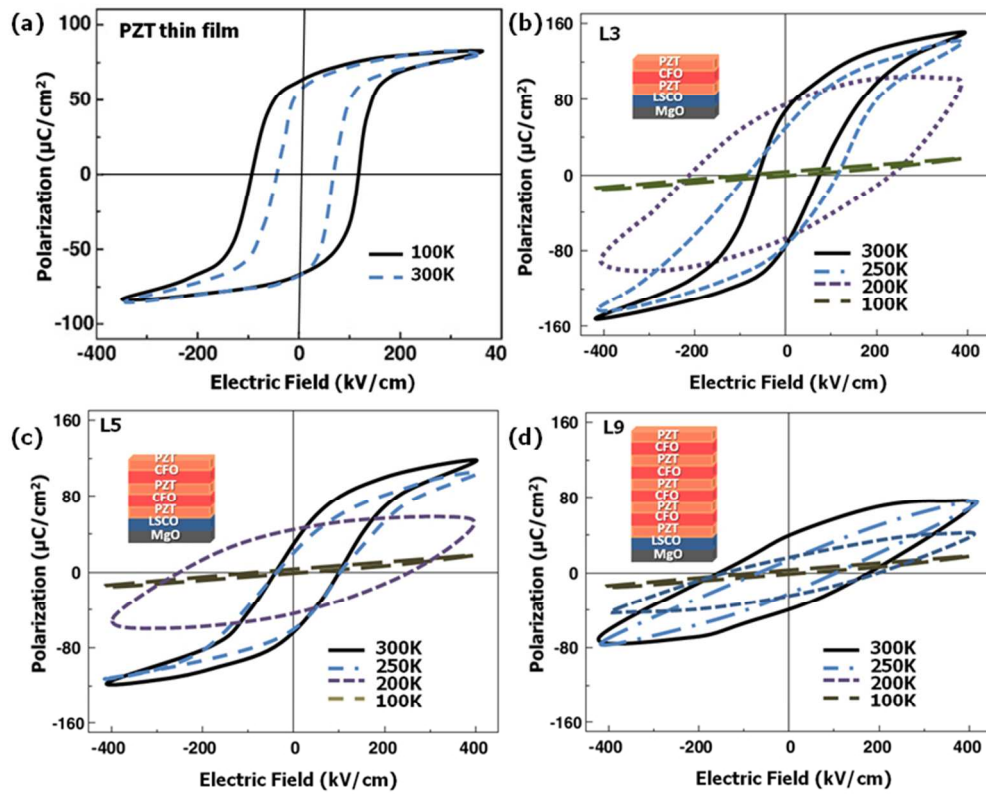
Figure 3: (a) Isothermal unipolar electric polarization versus electric field (P - E) hysteresis loops (b) temperature versus entropy (T - S) curves for a ferroelectric refrigeration cycle (A-B-C-D) operated between different temperatures T_L and T_H .

Figure 4: Schematic of refrigeration cycle based on reversed Olsen cycle. Note: $P_B > P_A > P_C > P_D$; $S_D > S_A > S_C > S_B$.

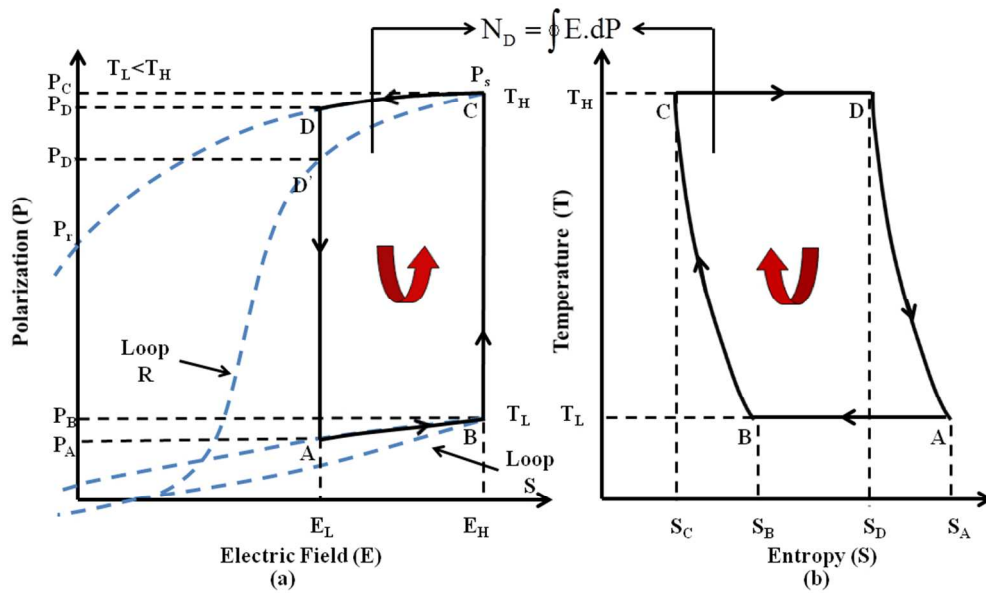
Figure 5: P - T plots for (a) L3, (b) L5 and (c) L5 corresponding to selected applied electric fields.

Figure 6: The variation in thermodynamic attributes (entropy (ΔS) and temperature (ΔT) change) with respect to temperature for selected applied electric fields (calculated using Maxwell relations-equations 1 and 2). The negative values indicate a negative ECE.

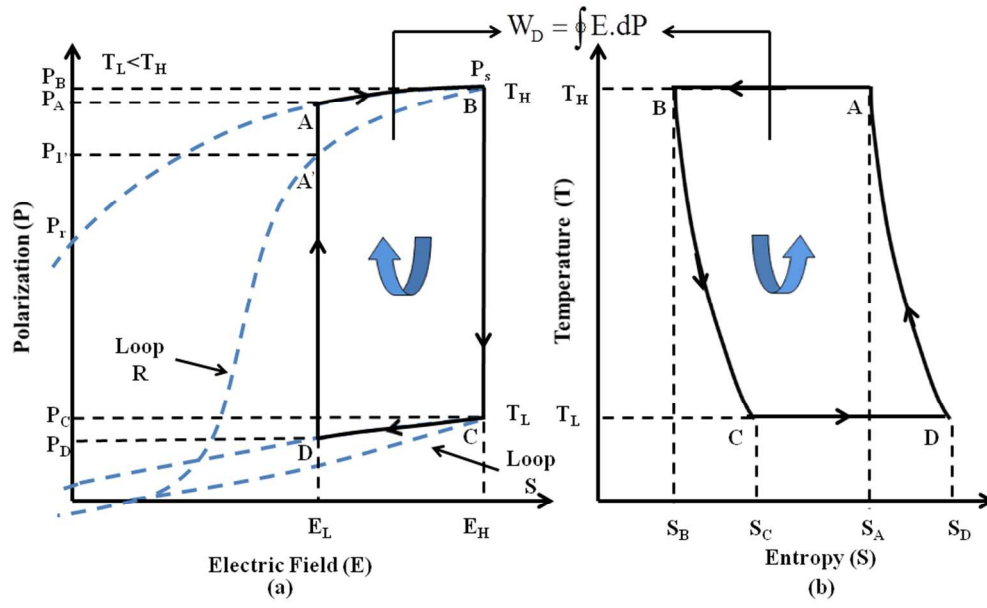
Figure 7: (a) The comparison of energy densities for all three configurations as a function of E_H in the temperature domain of 100-300 K; the variation of energy density (calculated using equation 5) as a function of E_H and T_H for (b) L3, (c) L5 and (d) L9 MLNs respectively. E_L is kept constant as 0 kVcm^{-1} .



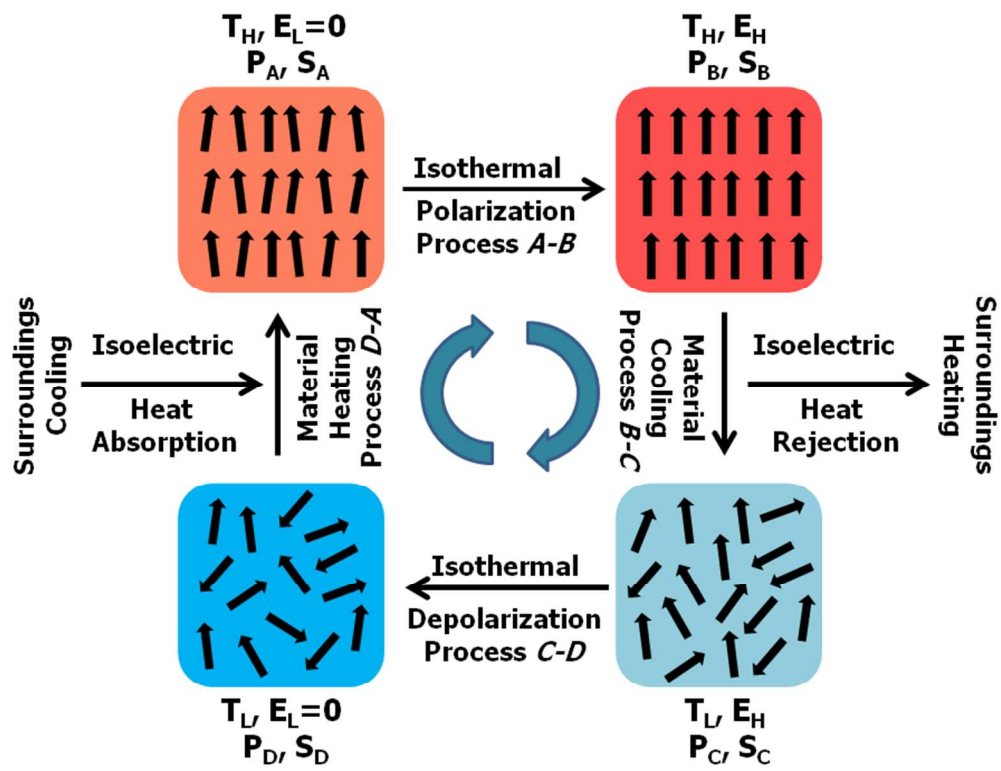
226x183mm (96 x 96 DPI)



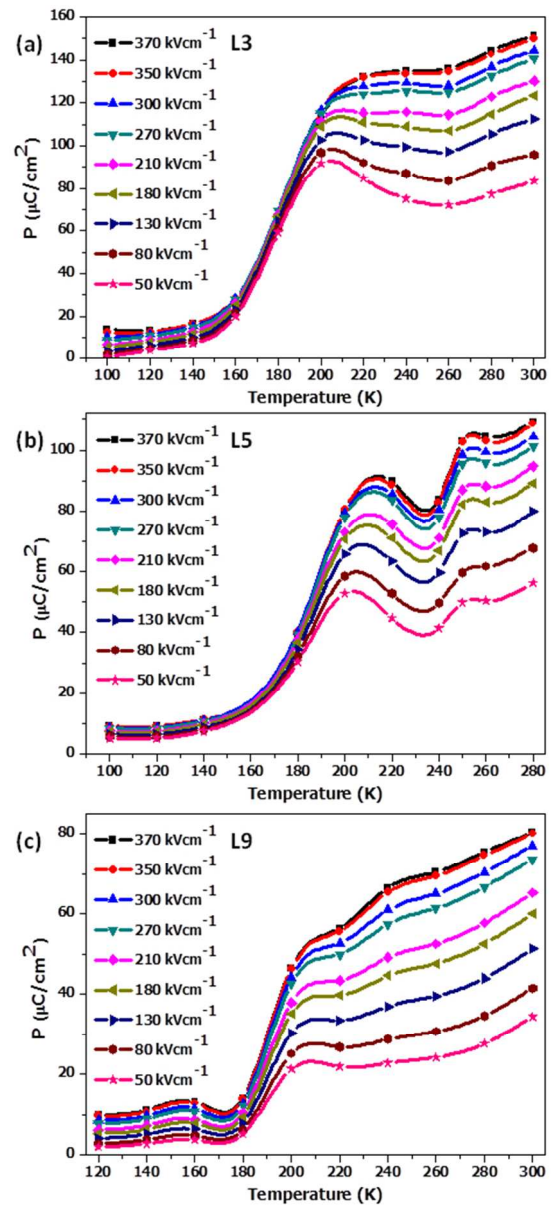
285x168mm (96 x 96 DPI)



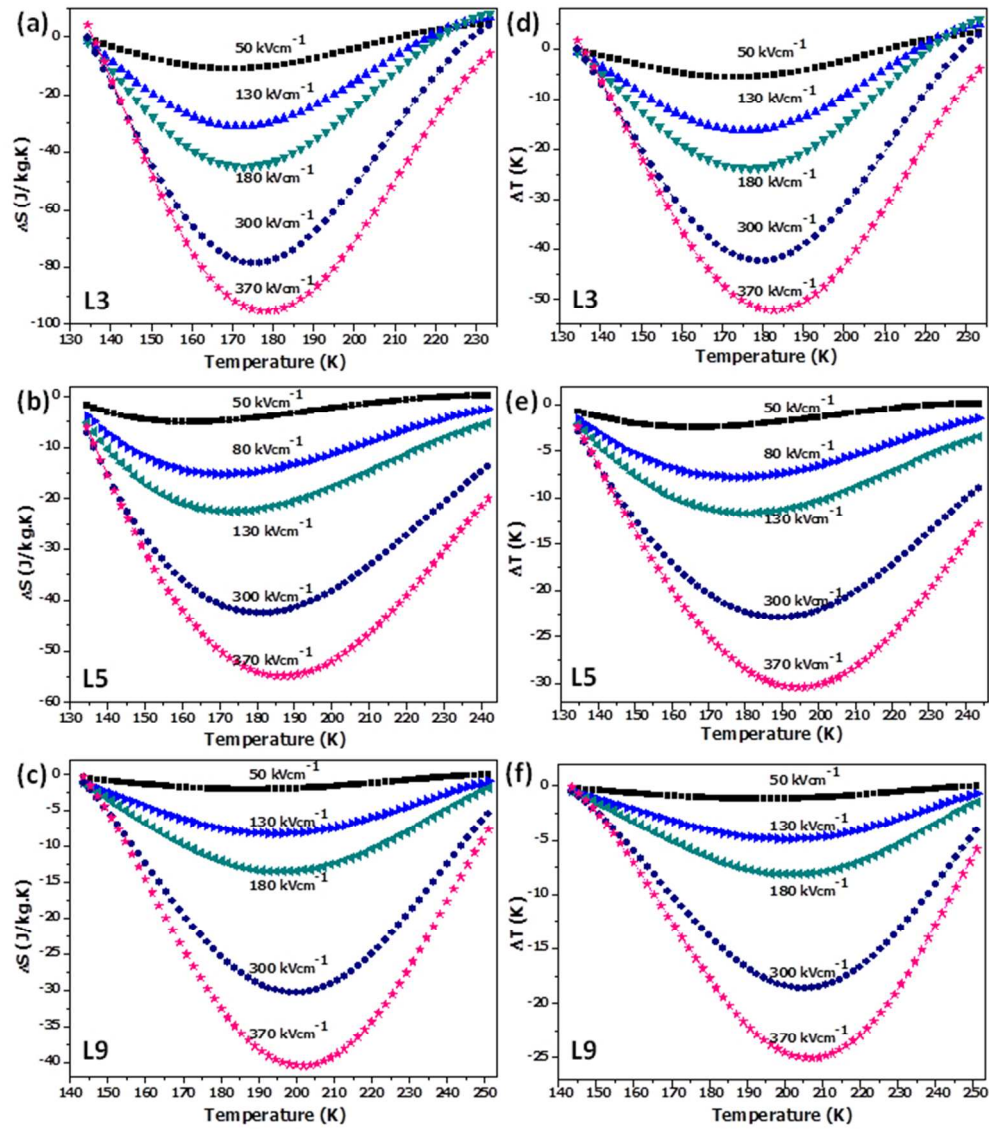
281x169mm (96 x 96 DPI)



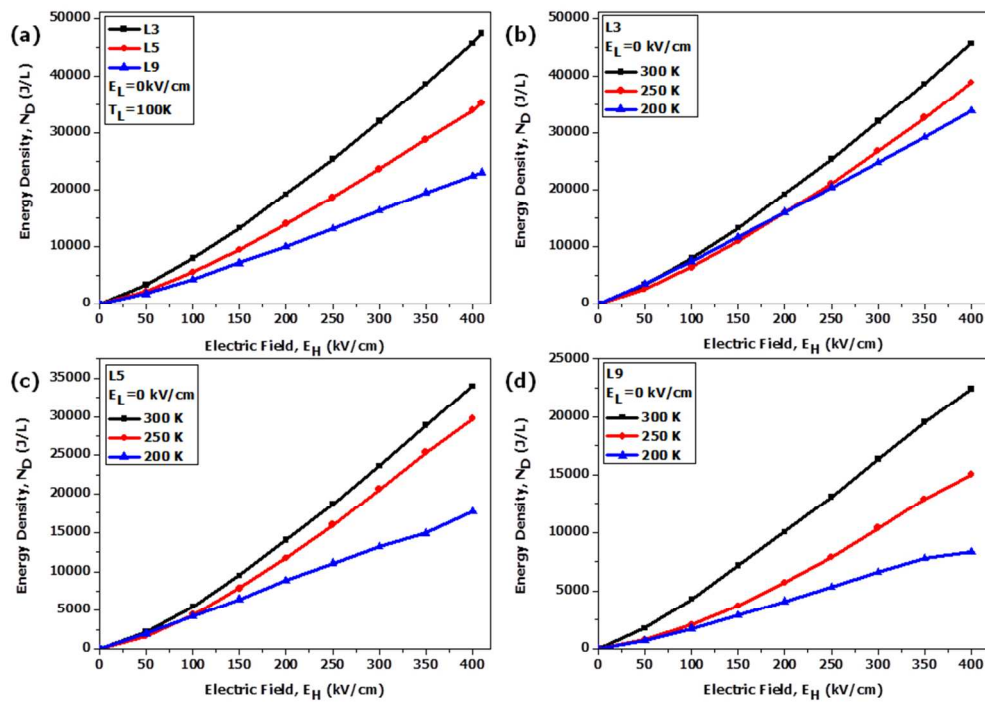
237x187mm (96 x 96 DPI)



126x272mm (96 x 96 DPI)



190x217mm (96 x 96 DPI)



250x177mm (96 x 96 DPI)